

1 **Impact of nested moisture cycles on coastal chalk cliff**
2 **failure revealed by multi seasonal seismic and**
3 **topographic surveys**

4 **M. Dietze¹, K. L. Cook¹, L. Illien¹, O. Rach¹, S. Puffpaff², I. Stodian², N.**
5 **Hovius^{1,3}**

6 ¹GFZ German Research Centre for Geosciences, Section 4.6 Geomorphology, Potsdam, Germany

7 ²National Park Authority Vorpommern, Research and Monitoring Division, Jasmund, Germany

8 ³Institute of Geosciences, University of Potsdam, Germany

9 **Running title:** Salmonid redd building seismology

10 **Key Points:**

- 11 • Multi-year UAV and seismic monitoring yielded a catalogue comprising timing,
12 propagation, and location of 81 coastal cliff failures
- 13 • Failures are controlled by water availability through subsurface flow, rain, and at-
14 mospheric moisture condensation
- 15 • Failures are controlled on diurnal, monthly, seasonal and multi-year scales

Abstract

Cliff failure is a fundamental process shaping many coastlines worldwide. Improved insight into direct links between cliff failure and forcing mechanisms requires precise information on the timing of individual failures, which is difficult to obtain with conventional observation methods for longer stretches of coastline. Here we use seismic records and auxiliary data spanning 25 months to precisely identify and locate 81 failure events along the 8.6-km long chalk cliff coast of Jasmund, on Germany's largest island, Rügen. The sub-minute precision of event timing allows the linkage of individual failures to triggers over a wide range of relevant time scales. We show that during the monitoring interval, marine processes were negligible as a trigger of cliff failure, although still being important for the removal of resulting deposits. Instead, cliff failure was associated with terrestrial controls on rock moisture. Most failures occurred when water caused a state transition of the cliff forming chalk, from solid to liquid. Water content was modulated by: i) subsurface flow towards the cliff, ii) rain onto the cliff, and iii) condensation of atmospheric moisture, leading to clustered failures preferentially during the night. Seasonal water availability, controlled by plant activity, imposed an annual cycle of cliff failure, and wetter and drier than average years imposed a month-long legacy effect on cliff failure dynamics. Similar terrestrial control mechanisms may also be relevant for other coastal chalk cliffs, in addition to already investigated marine triggers.

Plain Language Summary

Cliffs line many coastlines worldwide. They are eroded by cliff falls, with consequences for human safety, land loss, ecosystem dynamics and availability of sediment along the coast. The discrepancy between rapid, short-lived failure processes and episodic observation techniques does not allow for a full analysis of the causes and drivers of cliff erosion. Combining measurements from a seismometer network on Germany's largest island, Rügen, with 3D models from drone surveys and weather station data, we detected, located and timed 81 cliff failures in two years, and analysed the circumstances that gave rise to their occurrence. These events were predominantly associated with the presence of water, which turns the solid, cliff-building chalk into a failure-prone slurry. Water availability is modulated at different time scales by rain on the cliff and moisture condensation, soil water flow, vegetation water uptake, and possibly the lunar cycle. Our findings sharpen the picture of when and why cliffs fail, and offer a better prediction of the impact of global change on cliff coasts.

1 Introduction

Coastlines host about 40 % of the world's global population along with key infrastructure, cultural heritage and unique ecosystems (Menatschi et al., 2018). Coastal change can have a profound impact on these assets. Around half of the world's coasts consist of eroding cliffs (Young & Carilli, 2019). On these coasts, cliff failure occurs across a range of scales and by a multitude of processes acting on the different materials that form cliffs (e.g. Duperret et al., 2005; Kogure et al., 2006; Collins & Sitar, 2008; Stephensen, 2014; Rosser et al., 2013). A fundamental mechanism of coastal retreat worldwide, cliff failure is driven by cyclic loading and activation due to climate-driven processes. After a preparation phase, during which a cliff section is driven to instability, for example by weathering, propagation of discontinuities, undermining at the cliff base, or simply by static loading (Duperret et al., 2005; Kogure et al., 2006), failures can be initiated by a variety of trigger mechanisms. These include impact of tide- and storm-driven waves that exert forces on the cliff, entrain abrasive sediment and change the cliff geometry, for example through undermining (Collins & Sitar, 2008; Stephensen, 2014), wind-induced stress (Vann Jones et al., 2015) amplified when interacting with trees (Dietze, Turowski, et al., 2017), frost shattering or ice segregation and freeze thaw cycles (Letortu et al., 2015),

66 and rainfall and groundwater recharge causing gravitational loading and reduced shear
67 strength due to increased pore water pressure (Stephensen, 2014). In addition, failures
68 can cause further failures, leading to upward propagation of cliff erosion with time (Rosser
69 et al., 2013). Finally, there may also be failures that appear to happen without any clearly
70 attributable trigger mechanism, or with a trigger that a study design has not accounted
71 for.

72 Robust attribution of cliff failure to a particular triggering process depends on pre-
73 cise knowledge of the timing and location of the event, and of the preceding and con-
74 current conditions. Cliff failure is generally a rapid process once initiated, and relevant
75 conditions can change on short time scales (minutes to days). Therefore, especially for
76 large failures, triggers can remain difficult to identify or to link with the actual process
77 (Collins & Sitar, 2008; Rosser et al., 2013). Many past studies have used records of cliff
78 failure with monthly or coarser time resolution (e.g. Lim et al., 2010; Vann Jones et al.,
79 2015). While these studies have yielded valuable insights, data with hourly or better res-
80 olution may help to robustly constrain causal links. In this context, environmental seis-
81 mology offers a useful approach, because of its ability to deliver both high time resolu-
82 tion (at least sub-minute) and scalable location precision (usually 5–10 % of the inter-
83 station distance) for individual cliff failures.

84 Networks of seismic sensors can be used to detect, locate, and estimate the volume
85 and anatomy of mass movements at the landscape scale (e.g. Helmstetter & Garambois,
86 2010; Hibert et al., 2011; Burtin et al., 2016). The size limit of detection with a network
87 with a given station spacing and instrument configuration is set by the ambient noise
88 level, and depends on the transfer of energy from a mass movement into the substrate,
89 as well as on ground properties that determine the propagation and attenuation of the
90 resulting seismic waves. Dietze, Mohadjer, et al. (2017) were able to seismically detect
91 rockfall volumes as small as 0.05 m^3 with a fall height of less than 50 m, and to locate
92 them with deviations from independently constrained positions of about 80 m on aver-
93 age (7 % of the mean station spacing). This means that while discrete, failure-based ero-
94 sional fluxes can be tackled by the seismic approach, the diffuse part of an erosional bud-
95 get remains elusive. The main strength of this approach, however, is the continuous tem-
96 poral coverage of a larger area and precise time information for the onset and duration
97 of discrete events. The high temporal resolution of seismic data is a key to identifying
98 sensible triggers of failures by systematically measuring time lags between potential trig-
99 gers and recorded geomorphic processes (e.g. Dietze, Turowski, et al., 2017).

100 In this study we explore the drivers and triggers of coastal cliff failures on the Jas-
101 mund peninsula, part of Germany’s largest island, Rügen. We use seismic and unmanned
102 aerial vehicle (UAV) monitoring to detect, date, locate, verify and quantify cliff failures
103 over a period of two years. We analyse the spatial and temporal patterns of cliff failure
104 in the context of marine, meteorological, biological and hydrological boundary conditions
105 across scales from minutes to years. This yields quantitative constraints on the relevance
106 of triggers and drivers at distinct time scales.

107 **2 Materials and methods**

108 **2.1 Study site and instrumentation**

109 The study area on the Jasmund peninsula of Rügen comprises an iconic cliff coast
110 section with a length of 8.6 km. The cliffs are steep ($57_{-4}^{+8} \text{ }^\circ$, median and quartiles – used
111 here and throughout to account for non-normally distributed data) to partly overhang-
112 ing and up to 118 m high (48_{-13}^{+13} m). They are facing the Baltic Sea to the northeast,
113 a semi-enclosed basin with a minimal tidal range (about 15 cm, IZW, 2003). Located
114 in a National Park the area has been covered by a beech forest for more than 1000 years.
115 The local weather is dominated by an oceanic regime (DWD, 2019), with less than $5 \text{ }^\circ\text{C}$

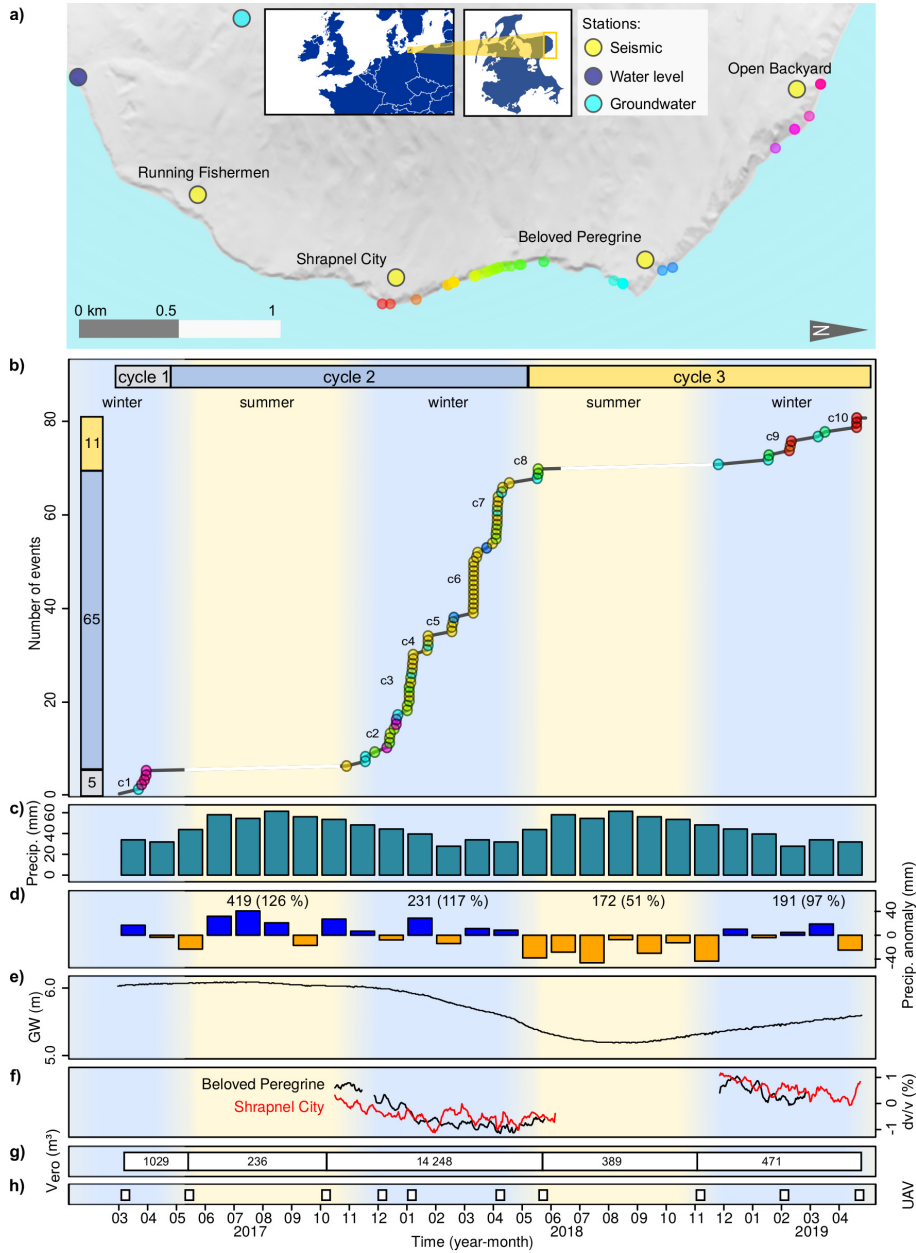


Figure 1. Study area and data sets. a) Hillshade map of study area with seismically detected failures (coloured by location). b) Failures with numbered event clusters. Vertical and horizontal bars denote seasonal cycles with cumulative number of failures per cycle. Circle colour corresponds to locations in (a). White line sections depict periods without seismic data coverage. c) Monthly 30 year average precipitation sums (DWD, 2019). d) Precipitation deviations from monthly averages. Numbers denote precipitation sums per season, indicated by yellow and blue background colours. Values in parentheses denote relative deviations from 30 year averages. e) Groundwater level (STALUVP, 2019) above 108 m asl. f) Seismic wave velocity changes (dv/v). g) UAV based failure volume sums per season. h) UAV flight dates.

116 diurnal air temperature range, positive mean monthly air temperatures throughout the
117 year (7.9 °C annual average, ranging between 0.2 and 16.5 °C) and 286 mm precipita-
118 tion during summer (defined in this study between May and October) versus 236 mm
119 during winter (defined here between November and April), resulting in 522 mm annual
120 average, and ranging between 27 and 60 mm/month. Access to this area is limited and
121 restricted to the existing trails, and a human role in triggering cliff failure in the area
122 can mostly be excluded.

123 The Jasmund cliffs have formed in weakly cemented Maastrichtian chalk, which has
124 been folded and thrust by the Scandinavian ice sheet into a sequence of stacked blocks
125 and covered by till (Gehrmann, 2018). Water content has an important effect on the sta-
126 bility of chalk in general and chalk cliffs in particular (Duperret et al., 2005; Obst & Schütze,
127 2005; Voake et al., 2019). The plasticity index (I_p), a classic measure of rigidity in en-
128 gineering geology (Williams, 2016), of the chalk bedrock of our study area is 7.8 ± 1.2 (pers.
129 comm. Christian Koepke, BAUGRUND Stralsund engineering office, 2019). This sug-
130 gests that water content changes of less than 10 % can have fundamental effects on the
131 state of the rock mass. In Rügen chalk, the transition from rigid to semi-rigid occurs at
132 22.0 ± 2.0 % and the transition to liquid at 29.8 ± 2.5 % water content. The average wa-
133 ter content of Rügen chalk is around 23 % (LUNG, 2019). Hence, the cliff material is
134 likely mostly in a meta stable state, and wetting and drying cycles may cause frequent
135 transitions between rigid, semi-rigid and liquid states. These material properties are con-
136 sistent with more detailed studies from northwest France, where chalk also forms sea fac-
137 ing cliffs. Duperret et al. (2005) found minimum natural water contents between 9.6 and
138 27 % (19 % on average) and measured strength reductions of 40–50 % when fresh wa-
139 ter was added to the chalk, and 52–73 % strength reductions for sea water uptake.

140 The Jasmund cliffs have retreated by erosion at about 25 cm/yr on average, gen-
141 erating a cumulative annual total of 103,000 m³ of debris along the coast section (Obst
142 & Schütze, 2005). This erosion estimate is based on Holocene time scale evidence and
143 allows for significant short-term variability. We note a similarity with rates of 25 cm/yr
144 for other regions with comparable cliff forming rocks, such as in northwest France (Duperret
145 et al., 2005), despite important differences in the wave and tidal energy of these coasts.

146 Between March 2017 and April 2019, we operated four seismic stations (Nanomet-
147 rics Trillium Compact 120s seismometers and PE6/B 4.5 Hz geophones, logged at 200
148 Hz by Digos DataCubes), at intervals of about 1.2 km along 7 km of the Jasmund cliff
149 coast. The sensors were deployed in 50 cm deep, hand dug pits, directly installed in the
150 outcropping chalk or till deposits, and mantled with fine sediment filled back into the
151 pit. Data loggers and 72 Ah lead batteries were kept in water proof plastic boxes, also
152 placed in hand dug pits about 50 cm next to the sensor, with only the GPS antenna look-
153 ing out to safeguard time stamp availability for the data. The system was able to op-
154 erate for about three months without data extraction and battery replacement mainte-
155 nance visits. Instrumentation was active during the autumn to late spring season, and
156 the sensors were dismantled during the summer period.

157 Repeat UAV surveys were used to generate high resolution 3D point clouds to quan-
158 tify topographic changes. These change data sets were used to verify seismic failure de-
159 tections and locations, to provide precise locations along the cliff, detachment heights
160 above the shore line and below the cliff top, and to estimate the volumes of failed ma-
161 terial. In addition, we used the UAV data to quantify failure volumes during the sum-
162 mer periods, for which no seismic data were available. Surveys (Fig. 1 h) were performed
163 using consumer-grade DJI UAVs, including a Phantom 3 Advanced (March 2017, May
164 2017, December 2017), a Mavic Pro (October 2017, January 2018, April 2018, May 2018),
165 and a Mavic 2 Pro (November 2018, February 2019, April 2019). Each survey consisted
166 of multiple flights from up to seven locations along the cliff, yielding 1000–2000 photos
167 for a full survey. The December 2017, January 2018 and April 2018 surveys were par-
168 tial surveys, covering the most active cliff sections between and about 500 m beyond the

169 two central seismic stations. The UAVs were flown manually and set to take photographs
 170 every three seconds. For a given survey, each section of the cliff was covered by at least
 171 two passes of the UAV with different flight elevation and camera obliquity. Camera an-
 172 gles typically ranged from 40–80 degrees from nadir, and elevations from 30–150 m above
 173 sea level. The distance between the camera and cliff varied depending on cliff height and
 174 weather conditions.

175 In addition to the seismic and UAV information, we used weather data at hourly
 176 resolution from the Arkona station of the Deutscher Wetterdienst, 20 km to the north-
 177 west (DWD, 2019), sea level data with minute resolution (WSV, 2019) from a gauge at
 178 the southeast limit of the study area in Sassnitz (Fig. 1 a), and daily groundwater data
 179 (STALUVP, 2019) from a well in chalk material 1.5 km west of the cliff coast (Fig. 1 a).
 180 For subsequent analyses (see section 4.3), we also used the HORIZONS web interface
 181 (JPL, 2019) to retrieve hourly lunar Ephemerides (data of the distance between the study
 182 area and the Moon’s centre of gravity).

183 2.2 Data processing

184 Seismic data were processed with the R package ‘eseis’ v. 0.5.0 (Dietze, 2018a, 2018b).
 185 Typical seismic waveforms of gravitational mass wasting events are spindle shaped (Hibert
 186 et al., 2011), and registered at seismic stations with a few seconds offset across our lo-
 187 cal network due to the finite velocity with which the seismic waves travel through the
 188 ground (Fig. 2 f). To identify these discrete events in the continuous stream of seismic
 189 data, we used a STA-LTA picker (Allen, 1982). For details on the settings and param-
 190 eter constraints see Supporting Information (SI). We screened these events with a series
 191 of automatic rejection criteria, admitting only those that lasted between 1 and 180 s (as-
 192 suming that shorter cases are random signal coincidences and longer signals are caused
 193 by earthquakes or anthropogenic activity). We considered only events detected by at least
 194 three seismic stations (minimum required to locate an event), within 11 s (maximum time
 195 required for a seismic signal to travel through the network). All admitted events were
 196 manually checked for plausibility based on: i) consistent amplitude decrease across the
 197 network as expected for a local seismic source, ii) consistent signal arrival time delay across
 198 the network, indicative of a local source predominantly emitting surface waves, iii) an
 199 emergent onset and slow decay of the signal, as reported for many hillslope mass wast-
 200 ing processes (Helmstetter & Garambois, 2010; Hibert et al., 2011; Dietze, Mohadjer,
 201 et al., 2017), iv) absence of earthquake-like distinct arrivals of different wave types, and
 202 v) absence of tremor-like frequency patterns, often associated with overhead passage of
 203 aircraft (Meng & Ben-Zion, 2018).

204 Detected events that passed manual screening were located by migration of the de-
 205 convolved, filtered vertical component signal envelopes (Burtin et al., 2013; Dietze, Mo-
 206 hadjer, et al., 2017). The final location estimates are reported as projections along the
 207 coast. This is done only for failures whose 90 % confidence interval overlapped with the
 208 coast, which is the only likely area of active mass wasting in the otherwise gently undu-
 209 lating landscape. The migration approach requires an assumed seismic wave velocity. Here,
 210 we used an example failure (Fig. 2 f) for which we know the location independently, and
 211 minimized the deviation of the seismic location estimate from the known location. Mi-
 212 gration results also depend on the window with which the seismic data were filtered. There-
 213 fore, we have also tested the location deviation as a function of filter width. For this, we
 214 ran the optimization routine for different filter windows, keeping the lower corner fre-
 215 quency constant at 5 Hz and gradually increasing the higher corner frequency from 6 to
 216 20 Hz. All detailed processing steps are described in the SI, including annotated R scripts.

217 Seismic wave velocities vary in time, as the mechanical properties and water con-
 218 tent of their medium change (Larose et al., 2015). Seismic noise cross correlation anal-
 219 ysis can be used to infer changes in the relative seismic wave velocity (dv/v), and thereby

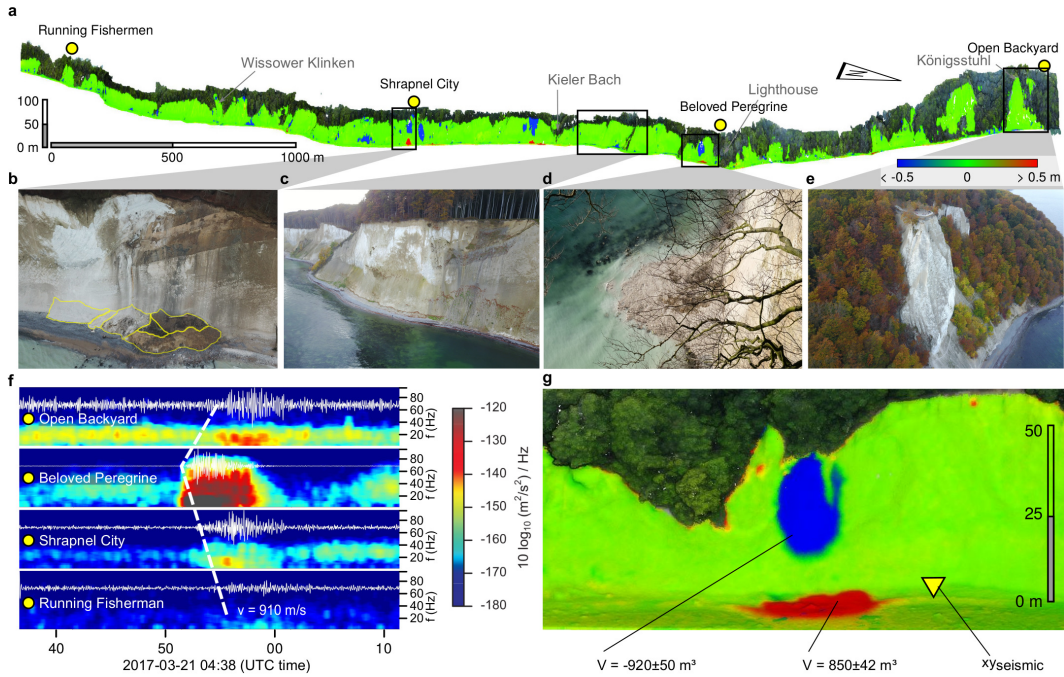


Figure 2. Cliff failure locations, anatomy and deposits. a) UAV-based cliff activity for the entire study period, shown as perspective oblique view from the sea. Tree carapace is shown in natural dark green colour. Colour bar indicates surface change in m. b) Site that exhibited repeated failure activity with discrete sub-deposits (yellow polygons), below station "Shrapnel City". c) Perspective view along the cliff towards the south with sequence of stacked chalk units. d) Terrestrial picture of recently failed site close to station "Beloved Peregrine". Note the suspension plume originating from failure deposit as direct consequence of waves incising the material reaching beyond the beach zone. e) The Königsstuhl, highest part of the cliff section under survey. f) Failure from d) as recorded by the seismic stations with an apparent wave velocity of 910 m/s. The 5–10 Hz filtered signals with their spindle-shaped evolution in time are plotted on top of spectrograms. g) UAV-based volume changes for the failure in d), based on UAV data from March and May 2017; perspective from the sea. Yellow triangle depicts best match seismic location, about 37 m north of the UAV based location. For enlarged versions of photos in b)–e) see SI.

220 to monitor the properties of the local substrate (Snieder, 2004). We determined dv/v
 221 for the two central stations ("Beloved Peregrine" and "Shrapnel City", all named after
 222 specific deployment characteristics) with the MIIC package (Sens-Schönfelder, 2014). Hourly
 223 signals were processed by filtering (4–8 Hz), spectral whitening, clipping at two standard
 224 deviations and sign-normalization, and the cross correlation functions were stacked to
 225 daily data. These results were converted to dv/v values using the stretching technique
 226 of Sens-Schönfelder and Wegler (2006). For mathematical background see SI.

227 UAV data processing was done using Agisoft Photoscan (v. 1.4.2) structure from
 228 motion (SfM) software. The cliff was split into five overlapping segments in order to re-
 229 duce processing time. We were unable to deploy or measure ground control points for
 230 the cliff surveys because of the National Park status of the study area, the inherent dan-
 231 ger of failures preventing us from accessing the beach, and dense vegetation cover and
 232 danger of failure of the overhanging top parts of the cliff. Thus, the surveys were geo-
 233 referenced using only the GPS data recorded by the UAVs. In order to obtain reliable
 234 change detection results, we followed the co-alignment workflow introduced in Cook and
 235 Dietze (2019). For each pair of surveys that were compared, we combined photos from
 236 both surveys for point matching, initial bundle adjustment, and optimization (follow-
 237 ing removal of tie points with reconstruction uncertainty ratio > 50). The two sets of
 238 photos were then separated for the dense cloud construction. Parameters for alignment
 239 were: high quality, key point limit of 40000, tie point limit of 4000, and adaptive cam-
 240 era model fitting. Parameters for dense cloud construction were: medium quality and
 241 aggressive depth filtering. The dense point clouds were compared using the M3C2 al-
 242 gorithm (Lague & Leroux, 2013) in CloudCompare (GPL, 2019) using the parameters:
 243 core point spacing 0.25 m, projection diameter 0.5 m, and normal scales 0.5 m to 4.5 m
 244 in 1 m steps. The accuracy of the resulting change cloud was assessed using the calcu-
 245 lated changes in the stable areas of the cliff (typically the majority of the cliff face). We
 246 estimate a level of detection of 10–15 cm or better for our change maps.

247 We manually inspected each of the change maps in concert with the available be-
 248 fore and after photographs to identify cliff failures. For each identified failure, we clipped
 249 the before and after point clouds to the area of measured change and calculated the vol-
 250 ume using the 2.5D volume tool in CloudCompare. We calculated each volume three times
 251 using the X, Y, and Z reference planes to determine the most appropriate reference plane
 252 for a given failure and estimate a relative volume uncertainty (9.7 % on average). In ad-
 253 dition, we estimated the elevation of the centre of each failure to give the height above
 254 the shoreline and the vertical distance from the cliff top.

255 **2.3 Estimation of seismic detection limit**

256 A cliff failure will only be detected when it emits sufficient kinetic energy to the
 257 ground. Since we need such a signal to be recorded by at least three seismic stations to
 258 locate the seismic source, the energy must be large enough to allow signal propagation
 259 over at least twice the average seismic station distance (1.2 km). On 26 January 2019
 260 National Park staff cut trees along the main road crossing the forest. The felling sites
 261 were between 2.0 and 2.5 km away from the closest three seismic stations of our coastal
 262 array. Forest staff confirmed that the largest trees had masses of up to 10 t and heights
 263 of up to 30 m. During this felling period, we had a further seismic station ("Fairground
 264 Attraction") running in the study area, located 1.7 km northwest of the station "Shrap-
 265 nel City", recording with the same instruments and parameters as the other stations (Fig. 4).
 266 We screened the seismic records of all stations during the tree felling to obtain conser-
 267 vative estimates of the minimum detectable volume of chalk material failing along the
 268 cliff. Therefore, we assume that maximum energy can be delivered to the ground if a tree
 269 would fall without any internal absorption of energy by swaying and bending branches,
 270 and treat a tree fall as free fall process of the entire tree mass from the mean tree height.

We were able to detect a series of at least 15 seismic signals (see Fig 4 for an example). The signal amplitudes were always recorded well above background noise levels at all operating stations, by a factor of 5 to 30, and the sources were, in many cases, located along the road where the trees were being cut. In the extreme case, a 10 t tree (based on the estimates of National Park staff and a specific density of the wood of about 1000 kg/m^3), falling freely from an altitude of 15 m (half the stem height), and without impact damping by branches, litter or loose soil, generated a seismic signal that can be detected by stations of our seismic array at a distance of at least 2.5 km. Such a mass would correspond to a chalk volume of 4 m^3 falling from a height of 15 m, given a density of chalk of $2,500 \text{ kg/m}^3$. The distance between our stations and the monitored cliff section is considerably smaller, and the true limit of systematic detection is thus likely lower.

2.4 Trigger analysis

A wide range of triggers may cause rock slope failure. From this range we can exclude geophysical (earthquake, volcanic eruption; Hibert et al., 2014) and other gravitational processes (snow avalanches, ice falls, debris flows; Stock et al., 2013) due to the location of the study site. Biological or anthropogenic triggers (animal traffic, human activities; Wieczorek, 1996) are unlikely in a protected area with virtually no access to the cliff face or any macro fauna activity along it. Thermal dilation and contraction (Stock et al., 2013; Collins & Stock, 2016) are assumed to play a subordinate role in generating stress cycles within the rock mass, given that the northeast-facing aspect of the cliff prevents intense and prolonged exposure to direct sunlight, especially during winter time. The daily amplitude of air temperature was $3.7_{-1.1}^{+1.3} \text{ }^\circ\text{C}$ for the entire study period, with even lower amplitudes during the November–May period ($3.1_{-0.9}^{+1.3} \text{ }^\circ\text{C}$). Since the propagation of temperature changes into the ground is associated with significant attenuation of the amplitude within a few cm (e.g. Holmes et al., 2008), and mechanical tests of the temperature effect on the tensile strength of chalk (e.g. Voake et al., 2019) showed only minimal effects compared to the impact of wetting, we consider it unlikely that such small air temperature amplitudes play a primary role in affecting the chalk material properties. Similarly, the tidal range of the Baltic Sea is about 15 cm, equivalent to the diameter of larger sediment clasts on the beach at the foot of the cliff. Moreover, in many places the beach forms a ramp of 2 m height from the water line to the cliff base. Thus, we consider tidal effects unlikely to be a dominant process affecting cliff failure.

Geotechnical measurements suggest that, under normal conditions, the chalk rock mass of the Jasmund peninsula may be close to or beyond a transitional state (rigid to semi-rigid or even liquid), and addition of comparatively small amounts of water may have significant effects on the stability of landforms built by this material. With the concept of a system sensitive to water content in mind, we focused our exploration for likely triggers of cliff failure on precipitation, wind, freeze-thaw transitions, sea level and wave action (Kennedy et al., 2017; Dietze, Turowski, et al., 2017).

We assessed the relevance of these trigger types by analysis of the time difference between a failure and the preceding trigger occurrence (Dietze, Turowski, et al., 2017). This assumes that a geomorphic response occurs while a trigger is active or after it has been active, either without delay or with a trigger-specific time lag (cf. Dietze, Turowski, et al. (2017) for detailed discussion of expected time lags). The resolution of any trigger analysis is limited by the resolution of both event timing and trigger proxy data. With our seismic detection methods, we are able to achieve at least sub-minute resolution of event timing, rendering trigger proxy timing ($< 1 \text{ h}$) the limiting factor.

To evaluate the role of precipitation in triggering of cliff failures, we calculated time lags with rain fall of 0.1 mm/h (the smallest measurement increment), 0.2 mm/h (quantile_{0.05} of the range of recorded rain intensities), and 0.5 mm/h (quantile_{0.10}). Further thresh-

322 olds could be included but would most likely result in systematically changing time lags
 323 as during rain storms the rain intensity is temporally autocorrelated. For wind, we de-
 324 fined wind events as episodes with one-hour average wind speeds at Beaufort scale 6, la-
 325 belled "strong wind", or higher. Freeze-thaw episodes were defined as transitions from
 326 negative to positive Celsius near-ground air temperatures, acknowledging that heat dis-
 327 sipation into the ground can take several hours (Dietze, Turowski, et al., 2017) and that
 328 there may be differences in air temperature between the study site and the meteorolog-
 329 ical station. The role of sea level as a direct trigger of cliff failures (i.e., minimal time
 330 lags) was assessed by calculating time lags for levels corresponding to the quantiles_{0.75,0.90,0.95}
 331 of the full distribution of sea level data (i.e., 16, 26 and 33 cm above average sea level,
 332 respectively). In the absence of wave buoy data, we cannot directly constrain wave height.
 333 Thus, we calculated the standard deviation of sea level in a moving window of 20 min,
 334 assuming that during storms higher wave amplitudes will result in greater standard de-
 335 viation values (i.e. increased variability of sea level around the mean).

336 The time lags for all triggers are visualized as kernel density plots, which provide
 337 a continuous representation of the empirical density distribution of the data, and are sim-
 338 ilar to histograms but without the bias created by definitions of bin sizes and class bound-
 339 aries (Dietze et al., 2016). We restricted the analysis to a maximum time lag of 72 h,
 340 assuming that all triggers operate at time scales shorter than three days. To estimate
 341 the significance of our analyses, we tested the time lag distributions resulting from the
 342 empirical failure catalogue for statistical difference from 1001 synthetic event data sets
 343 of the same size as the empirical catalogue. Each synthetic data set was generated by
 344 randomly assigning start times for the entire study period. We used the two-sample Kolmogorov-
 345 Smirnov (KS) test to evaluate whether the distributions are significantly different from
 346 random occurrence or not.

347 Although we do not have the same temporal resolution data between winter and
 348 summer for cliff collapse identification, the length of the monitoring period (25 months)
 349 allows us not only to investigate time lags to triggers, but also to identify activity vari-
 350 ations across time scales from diurnal to lunar orbital and annual. For these cycles we
 351 calculated spectra of the continuous time series of potential triggers and drivers. The
 352 discrete distribution of cliff failures was converted to a continuous distribution by cal-
 353 culating a kernel density estimate with hourly resolution and a window size of two days,
 354 and normalizing the resulting density values.

355 3 Results

356 3.1 Event detection, location and anatomy

357 Automatic picking of seismic events yielded a total of 2818 potential cliff failures.
 358 After manual screening and validating that seismic locations were along the coast, we
 359 confirmed 81 as likely actual cliff failures (Fig. 1). The 81 seismically detected failures
 360 (figures in SI A5) lasted in general $9.0^{+2.9}_{-2.0}$ s, almost exclusively with an emergent on-
 361 set, signal rise times (time from signal onset to maximum amplitude) of $2.8^{+1.5}_{-0.8}$ s and
 362 fall times (time from maximum amplitude to event end) of $6.7^{+2.0}_{-2.0}$ s. The signals had
 363 central frequencies of $15.9^{+6.6}_{-4.2}$ Hz. In 26 % of all cases, a failure was followed by at least
 364 one other event less than 200 m away within 24 hours. We recorded one event cluster
 365 composed of 11 discrete failures during 10.5 hours, starting on 2018-03-09 16:17:15 UTC
 366 (see Tab. SI 3).

367 We use an event on 21 March 2017 at 04:38 UTC time to illustrate the insights from
 368 combining the seismic monitoring and UAV surveying (Fig. 2 f–g). This failure, located
 369 about 200 m south of station "Beloved Peregrine", generated a seismic signal with an
 370 emergent onset, a rise time of 1.5 s, and a fall time of 7.3 s (see white signal time series
 371 on top of spectrograms in Fig. 2 f). Photographs taken by park authorities 3 days af-

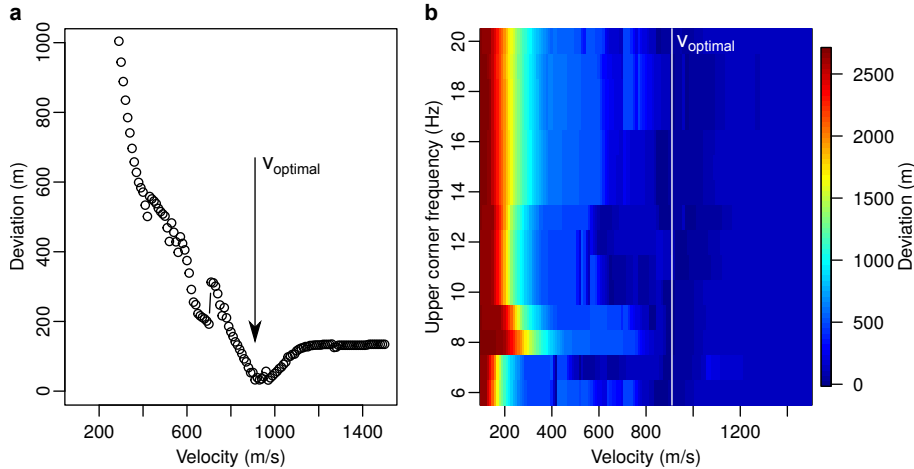


Figure 3. Estimate of apparent seismic wave velocity by minimization of model location deviations from empirically known location. a) Deviation as function of wave velocity for 5–10 Hz filtered signals. b) Deviation map resolving deviation as function of wave velocity and filter frequency width (5 Hz as fixed lower corner frequency). White vertical line depicts optimal velocity ($v_{optimal} = 910$ m/s) from (a) to illustrate the general agreement of this optimal value also for other frequencies.

372 ter the event confirmed it as a cliff failure involving around 800 m^3 of material that frag-
 373 mented during transport and covered the beach as a flow-like deposit, extending into the
 374 sea (Fig. 2 d). Our UAV-based change model, based on a survey in May 2017, shows a
 375 cliff failure with a volume of $920 \pm 50 \text{ m}^3$, located at 32 m above sea level, and a corre-
 376 sponding deposit of $850 \pm 42 \text{ m}^3$ (Fig. 2 g), not including material beneath the water level,
 377 thus rendering the mapped deposit volume a minimum estimate.

378 The optimal apparent seismic wave velocity for event location (Fig. 3) yielded a
 379 consistent value of 910 m/s regardless of the width of the filter window applied to the
 380 seismic data. For this seismic velocity, the location error was minimized at 37 m. As-
 381 suming constant conditions, we used this velocity value for location of all other detected
 382 failures.

383 Based on UAV-derived 3D models, we measured compound failure volumes between
 384 1.10 and 4985 m^3 ($20.0^{+35.8}_{-13.6} \text{ m}^3$). The cumulative detected failure volumes for the sea-
 385 sons with vegetation activity (May–October) were 236 and 389 m^3 in 2017 and 2018, re-
 386 spectively. For the non-vegetative seasons, the cumulative volumes were 1029 m^3 (2017,
 387 March–April), 14,248 m^3 (2018, November–April) and 471 m^3 (2019, November–April,
 388 cf. Fig. 1 g for a summary). In many cases the UAV imagery showed that new cliff base
 389 deposits were amalgams of multiple cliff failures (Fig. 2 b). Failures initiated at heights
 390 of $29.0^{+10.5}_{-16.0}$ m a.s.l. and $24.0^{+3.7}_{-9.0}$ m below the cliff top. Many failure scars and deposits
 391 were the result of multiple events. This prevented us from constraining the relationship
 392 between individual event seismic amplitudes and volumes, and precluded a robust volume-
 393 frequency analysis.

394 Screening for precursor activity during 60 minutes before the failures revealed ran-
 395 dom brief pulses of seismic activity at the closest station in a few instances (e.g., 18-04-
 396 09 19:04, 18-03-10 02:50, 18-03-09 23:34, 18-02-15 02:15, 18-01-01 02:17). We did not find
 397 a systematic increase in amplitude or decrease in recurrence time of these pulses towards
 398 the cliff failure.

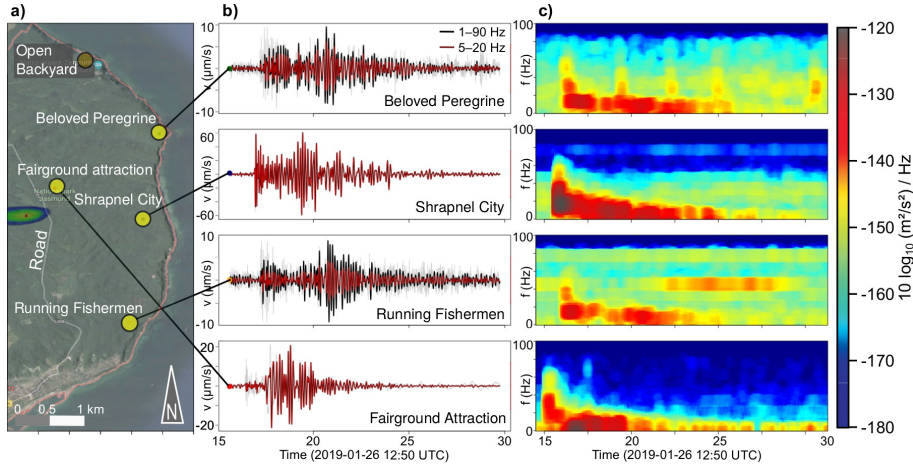


Figure 4. Seismic characteristics of a tree cutting process. a) Map (same extent as in Fig. 1 a) showing the location of the seismic stations used to analyse the event. Red line depicts coast outline. Note additional station close to main road only used in this experiment. Seismically determined location of tree cutting event is shown as coloured polygon with centre 100 west of the road, where the tree was actually cut. b) Seismic signals of the event at two different filter windows (black and red lines) and as unfiltered seismograms (grey lines). c) Seismic spectrograms of the signals.

399

3.2 Trigger time lags and activity cycles

400

401

402

403

404

405

406

407

408

409

410

411

412

413

We measured the time difference between the 81 recorded cliff failures and the preceding manifestation of a potential trigger, and label this the trigger time lag. Freeze-thaw time lags were considered within a 72-hour window. The time lags of the 20 failures that occurred within this window peaked around 48 h. Time lags for precipitation showed bimodal distributions for all three threshold values (0.1, 0.2, 0.5 mm/h) at 0–3 and 16–20 h, for between 62 and 67 out of the 81 failures depending on the rainfall rate. There is also a very suppressed third mode between 30 and 40 h. Time lags for wind showed a plateau between 1 and 10 h and secondary modes at 35–55 h for a total of 71 failures. Sea level time lags were 0–2 h for all three thresholds, applying to 17–30 failures. Sea level standard deviation within the 20 min moving window was $4.18^{+3.01}_{-1.54}$ cm (maximum 30.2 cm). Time lag analysis showed that only 7 (q_{75}) to 15 (q_{95}) failures had sea level-related time lags within 0–2 h during the three day period of interest. Except for wind, all time lag distributions were significantly different from random (i.e., Kolmogorov-Smirnov (KS) test D values > 0.24 and p values < 0.01 , see Fig. 5).

414

415

416

417

418

419

420

421

Failures showed a tendency to happen during night time hours. 50 failures occurred between 8 pm and 8 am, and 31 between 8 am and 8 pm (Fig. 6 b), but this variability is not significantly different from random ($D = 0.17^{+0.04}_{-0.02}$, $p = 0.18^{+0.16}_{-0.12}$). A diurnal pattern was also observed in air humidity, ranging on average between 75 % and 87 % over a day-night cycle in summer ($D = 0.38^{+0.08}_{-0.04}$, $p < 0.07$) and between 82 % and 90 % in winter ($D = 0.46^{+0.04}_{-0.04}$, $p < 0.002$). During days with failures, air humidity was especially high, between 85 % and 94 % ($D = 0.38^{+0.08}_{-0.04}$, $p < 0.07$), with peak values preceding cliff failure by 1–2 hours.

422

423

424

425

At the monthly scale, failures occurred more frequently when the moon was farther away from the cliff (Fig. 6 c; 65 versus 16 with respect to the average lunar distance). The lunar distance ranges from 350,000 to 410,000 km, a 14.4 % difference. Spectral analysis revealed statistically significant periodicity modes between 25 and 29 days for lu-

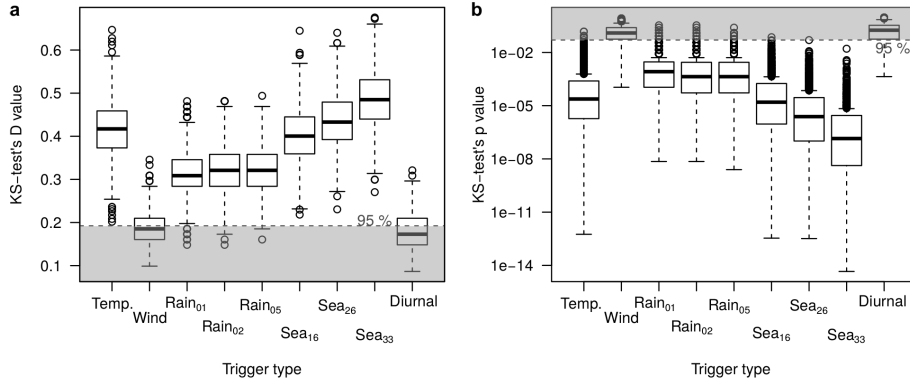


Figure 5. Statistical (Kolmogorov-Smirnov) significance tests for the triggers of cliff failures (Null hypothesis: random occurrence). a) D-values and b) p values for 95 % significance thresholds indicated by horizontal dashed lines. Grey shaded areas depict insignificant cases. Triggers are listed along the x axis, including freeze-thaw transitions (Temp.), high wind speeds (Wind), precipitation at three intensities (Rain₀₁, ₀₂ and ₀₅ mm/h), sea levels (Sea₁₆, ₂₆, ₃₃ cm above average), and preference of failures at night versus day time (Diurnal).

426 nar distance, precipitation and cliff failures (Fig. 6 d). The systematic relationship with
 427 cliff failure was only violated during the days around the year end 2017/18 (Fig. 6 c, clus-
 428 ter c3 in Fig. 1). That episode, with a total of 12 subsequent failures, seven of them at
 429 nearly the same location, was associated with persistent precipitation (31 mm in 7 days,
 430 compared to a 30-year monthly average of 46 mm).

431 Detected failure occurrence as inferred from seismic and UAV data was highly sea-
 432 sonal (Fig. 1 b and g) with most of the volume mobilized between November and April.
 433 In contrast, precipitation was stronger between May and October (331 mm versus 250
 434 mm). A cyclic trend was also observed in the seismic velocity data (Fig. 1 f) with high
 435 dv/v values during May and October, decreasing with the onset of late autumn. How-
 436 ever, this pattern was decoupled from the evolution of the groundwater level (Fig. 1 e).

437 Finally, during the instrumented period we have recorded the imprint of a compar-
 438 atively wet year with 121 % of the 30-year average precipitation, including 126 % for May
 439 to October 2017, followed by a drier-than-average year with precipitation totalling 74 %
 440 of the 30-year average, including a summer season with only 51 % of the average sea-
 441 sonal rainfall (Fig. 1 d). We have seismically detected 65 cliff failures during the winter
 442 season of the wet year, and only 11 failures in the winter season of the dry year.

443 4 Discussion

444 4.1 Propagation and spatial properties of cliff failures

445 The UAV-based failure heights ($20.0^{+35.8}_{-13.6}$ m³, following a log-normal distribution,
 446 with six volumes between 1.0 and 3.7 m³) were in general well above the estimated min-
 447 imum failure volume that can be detected seismically (about 4 m³). Any geometric bias
 448 in failure detection due to the seismic network layout was minimal for the central part
 449 of the cliff, where the distance to a set of three stations was less than 2 km throughout.
 450 Note, however, that this bias only potentially affects the event location, not the detec-
 451 tion limit. The size of our catalogue was small compared to catalogues from other ap-
 452 proaches (e.g. Lim et al., 2010; Vann Jones et al., 2015). Thus, our data did not allow
 453 for a meaningful evaluation of magnitude-frequency relationships or the role of small fail-

454 ures ($<4 \text{ m}^3$) in long-term cliff erosion, and we did not attempt a full erosional budget.
 455 However, the catalogue did permit the analysis of activity patterns along the entire cliff
 456 coast and an investigation of the kinetics of single failures, temporal clustering of cliff
 457 failures, and the links between failures and trigger mechanisms.

458 Recorded events had similar rise and fall times, durations and frequency contents
 459 of seismic signals. Combined with the UAV based locations at $29.0^{+10.5}_{-16.0}$ m above the cliff
 460 base and $24.0^{+3.7}_{-9.0}$ m below the cliff top (pointing at the mid-cliff area as preferred fail-
 461 ure sites), this suggests that the failures had comparable detachment and displacement
 462 processes. We observed predominantly spindle shaped seismograms, which reflect the avalanch-
 463 ing movement of fragmented chalk volumes that spread out at the cliff base. Many of
 464 the detected events were not intact block falls, which would produce single seismic pulses
 465 (Hibert et al., 2011; Dietze, Turowski, et al., 2017). These results were in agreement with
 466 observations of the example failure (Fig. 2). This event generated a deposit with a vol-
 467 ume of at least 850 m^3 , forming a radial sediment body that could be eroded and mod-
 468 ified by waves immediately. The erosive action of the Baltic Sea is visible in Fig. 2 d, where
 469 the deposit feeds a plume of bright chalk material into suspension.

470 During the survey period, recorded activity was focused predominantly in the cen-
 471 tral cliff section, between stations "Beloved Peregrine" and "Shrapnel City", with only
 472 7 failures outside this area (Fig. 1 a). This activity pattern is reflected in the shape of
 473 the different cliff sections. Between the two central stations, the cliff is steepest (46 ± 16
 474 $^\circ$ average slope), and has the most overhanging facets. It is mostly devoid of vegetation,
 475 and has waterfalls at the outlets of creeks. North and south of the two central stations,
 476 slopes are gentler, 38 ± 13 $^\circ$ and 41 ± 16 $^\circ$, respectively, and several channels have incised
 477 to sea level. This contrast suggests that activity segmentation manifests itself in the ge-
 478 omorphology, with failure-driven cliff retreat in the centre of the Jasmund coast and dif-
 479 fusive or catchment-confined hillslope sediment transport to the north and south. The
 480 reason for this segmentation of cliff shaping process combination remains elusive from
 481 our study design (time scale of surveying, measurement parameters included). While spa-
 482 tial differences in meteorological conditions, marine effects and landcover are unlikely
 483 to be significant, it may be the glacial thrusting dynamics that have generated an increased
 484 susceptibility of the central cliff section to water availability and flow below the surface.

485 4.2 Triggers of cliff failures

486 The seismic records were missing during the summer periods, but according to the
 487 UAV results, the total volumes of failures during summer were always lower than dur-
 488 ing winter periods. Without complete seismic information we cannot include the sum-
 489 mer periods in our subsequent trigger analysis, which introduces a possible seasonal bias.
 490 However, the UAV change detection results showed similar detachment elevations and
 491 deposit shapes throughout summer and winter seasons. Thus, we infer that unrecorded
 492 summer failures should be comparable to those for which we have seismic data.

493 Cliff failures were significantly linked with precipitation in about half of the cases.
 494 Time lags show two clusters, at 0–3 ($n = 19$) and 16–20 ($n = 20$) hours (Fig. 6 a).
 495 This suggests that rain may impact cliff stability through two different mechanisms. We
 496 interpret the rapid response as the effect of rain directly onto the cliff, and the delayed
 497 response as the consequence of water flow towards the cliff face within the soil covering
 498 the chalk landscape at the cliff top. Typical hydraulic conductivity values for unfractured
 499 Rügen chalk, $k_f \sim 10^{-10}$ m/s (Krienke & Koepke, 2006), allow flow rates of only a few
 500 micrometers per day, whereas the higher conductivity of the cover material, $k_f \sim 10^{-4}$
 501 m/s, theoretically permits water from up to 8.6 m hinterland to seep into the cliff face
 502 within a day. Note that seepage can have a longer range where preferential, lateral flow
 503 paths are present, for example along fractures and discontinuities, or in sediment-filled
 504 hollows.

505 We reject wind, sea level, waves, and freeze-thaw transitions as important triggers
 506 based on KS test results (Fig. 5, distance values D below and p-values above the 95 %
 507 significance threshold levels) and a lack of plausible mechanisms for the measured time
 508 lags. Wind time lags plateau between 0–10 h (Fig. 6 a) and within this window they are
 509 not distinct from random. We have not found a plausible mechanistic interpretation of
 510 this distribution, especially with failures predominantly occurring at $29.0^{+10.5}_{-16.0}$ m above
 511 the beach and $24.0^{+3.7}_{-9.0}$ m below the cliff top, and thus outside the range of processes at
 512 the cliff toe or the tree covered cliff top. Sea level time lags of 0–3 hours (for 17–30 out
 513 of 81 failures) are an effect of the seasonally changing sea level (514 cm in winter ver-
 514 sus 502 cm in summer), which results in winter cliff failures mapping onto higher sea lev-
 515 els. Wave amplitude variability (running window standard deviation of sea level) of a
 516 few cm, with a maximum of 30.2 cm, is one order of magnitude smaller than the height
 517 of the beach ramp. In this configuration, direct impact of waves on the base of the cliff
 518 is rare, and indirect impact will be damped by the coarse, unconsolidated beach sedi-
 519 ment. Moreover, the persistence of fine-grained deposits at the cliff base (Cook & Di-
 520 etze, 2019) throughout multiple UAV surveys (i.e. throughout several months) further
 521 indicates that waves have rarely impacted the base of the cliff during our study period.
 522 It is likely that waves have not acted as triggers of cliff failure over the monitoring in-
 523 terval. However, waves have played an important role in episodically removing the loose
 524 failure material from the base of the cliff (e.g., Rosser et al., 2013). Tides of $\tilde{15}$ cm ap-
 525 pear to be irrelevant given that the ramp of the shore platform has a height range of 1–
 526 2 m. In addition, most of the failures occur at $29.0^{+10.5}_{-16.0}$ m height above the beach, with-
 527 out indications of undermining at the base. Thus, we reject high sea levels and tides as
 528 trigger mechanisms for the documented failures. Freeze-thaw time lags of about two days
 529 (Fig. 6 a) render this mechanism an unlikely trigger because heat dissipation probably
 530 happens within hours rather than days (Dietze, Mohadjer, et al., 2017). A further po-
 531 tential cause for failures could be the occurrence of a previous failure, destabilizing the
 532 cliff’s stress field (e.g., Rosser et al., 2007). Indeed, we find that in 26 % of cases, an-
 533 other failure happened within 24 hours after a preceding one at or near the same loca-
 534 tion. However, the spatial confidence of the seismic location approach is too low to pur-
 535 sue this in the context of our network geometry and station spacing. Future studies en-
 536 gaging with this particular topic require denser instrument networks and higher sam-
 537 pling rates. Finally, note that there may be failures without any detectable (or detected)
 538 trigger mechanism (e.g. Stock et al., 2013), a phenomenon we also see in our trigger re-
 539 sults, specifically in the number of events within the trigger lag time analysis window
 540 (numbers in parentheses in fig. 6 a), which is always smaller than the size of the failure
 541 catalogue.

542 Precipitation is a typical cause of rock slope failure, but from our data we see a fur-
 543 ther aspect of water in the environment. Another (though not statistically significant)
 544 trend is that cliff failures occurred more frequently during the night (Fig. 6 b). Rain has
 545 a mostly uniform distribution throughout the day (Fig. 6 b), so cannot explain this di-
 546 urnal pattern of failures. During days with failures, recorded during the winter season,
 547 relative air humidity was systematically higher than during other winter days and es-
 548 pecially compared to summer season days (Fig. 6 b). Most importantly, cliff failure ac-
 549 tivity followed the daily relative humidity cycle with a time lag of 1–2 hours. Therefore,
 550 we propose that relative humidity may contribute to cliff activity at this time scale, even
 551 in the absence of rain. During the cooling hours at the end of the day, increased humid-
 552 ity and decreasing air temperature can lead to crossing of the dew point. Rates of dew
 553 formation on various surfaces range between 10^{-2} and 10^{-1} mm/h (Garratt & Segal, 1988),
 554 with controls exerted by meteorological conditions and surface properties. These dew
 555 formation rates can cause cumulative overnight water deposition at the same order as
 556 precipitation thresholds (0.1, 0.2, 0.5 mm/h) used in our trigger analysis. This water can
 557 migrate quickly into the fractured chalk at the cliff face and increase the water content
 558 of the material, possibly causing rheological changes.

559 We propose that the cliff failures observed during this study occurred primarily due
560 to wetting of the fractured chalk. This wetting can be due to rain directly onto the cliff,
561 subsurface flow towards the cliff, or condensation of atmospheric water vapour at the cliff
562 surface. Regardless of the pathway, increased water content can result in a sharp transi-
563 tion in rheological behaviour of the cliff-forming material, from rigid to liquid. Increased
564 water content contributes to failures by increased loading and shear strength reduction,
565 which adds to the instantaneous effect of the material state transition at the cliff face
566 upon sufficient wetting.

567 The absence of wave forcing in our study area allowed us to specifically study the
568 role of terrestrial drivers and triggers, at much greater detail and resolution than would
569 be possible in regions where marine processes play a significant role, as well. The pro-
570 posed moisture driven mechanism requires a rheological setting in which seasonal and
571 shorter term water content changes can cause material state transitions. Thus, while coastal
572 chalk cliffs are most likely prone to this effect, and cliffs with sandy or weakly consol-
573 idated material may undergo similar processes, more resistant lithologies such as lime-
574 stone or crystalline rock would be less prone to moisture driven failures. Since the chalk
575 properties in other coastal cliff landscapes (e.g., Duperret et al., 2005) do not differ sub-
576 stantially from the properties of our study site, moisture driven failure activity might
577 be a generic mechanism in such lithologies. However, unless studies at other sites also
578 utilise the information that can be provided by high resolution joint seismic and remote
579 sensing surveying, the relative contribution of cliff internal versus wave driven failure ini-
580 tiation remains obscured.

581 **4.3 Cliff activity at the lunar cycle**

582 The overlapping spectral peaks of cliff activity and lunar distance were unexpected.
583 At a first glance, one would expect lunar distance (JPL, 2019) to affect the net local grav-
584 itational force at the Earth’s surface, imposing dilation of bedrock, changes in pore space
585 and decreasing groundwater potential via tidal stress (e.g., Inkenbrandt et al., 2005).
586 However, effects on the net gravitational force are negligible: a 10^{-7} decrease of Earth’s
587 gravitational pull when the moon is closest to the study area. Similarly, tides in the Baltic
588 sea are small, and sea level does not appear to be a direct cause of detected cliff failures.
589 An influence of the moon on groundwater has been reported, although predominantly
590 on the diurnal and semi diurnal scale (Briciu, 2014). However, groundwater on Jasmund
591 did not show any significant lunar periodicity (Fig. 6 d).

592 Perhaps more relevant, Cervený et al. (2010) found a robust lunar signal in river
593 discharge across the United States, which they attributed to a precipitation cycle syn-
594 chronized with the lunar month. Such synchronous effects were also identified in other
595 settings around the globe (Bradley et al., 1962; Adderley & Brown, 1962; Roy, 2006; Leth-
596 bridge, 1990). Quoting Cervený et al. (2010) it emerges that “as a potential cause to these
597 previous findings of tidal forcing’s influence on precipitation and thunderstorms, past cli-
598 matological and astronomical research has proposed that the lunar synodic cycle may
599 be linked to (a) lunar distortion of the Earth’s magnetic tail [Lethbridge, 1970, 1990], (b)
600 the occurrence of cosmic rays [Markson, 1981], and (c) variations in meteoric dust [Adder-
601 ley and Brown, 1962] acting as condensation nuclei, among other explanations”. This
602 relationship is in line with our data showing agreement of significant spectral peaks of
603 precipitation, lunar distance, and cliff failures (Fig. 6 d). Thus, based on these findings,
604 we propose that lunar cyclicity may affect cliff failures indirectly, through the mediat-
605 ing role of precipitation. Obviously, longer time series with more precisely dated failures
606 are needed to better constrain this proposed relationship.

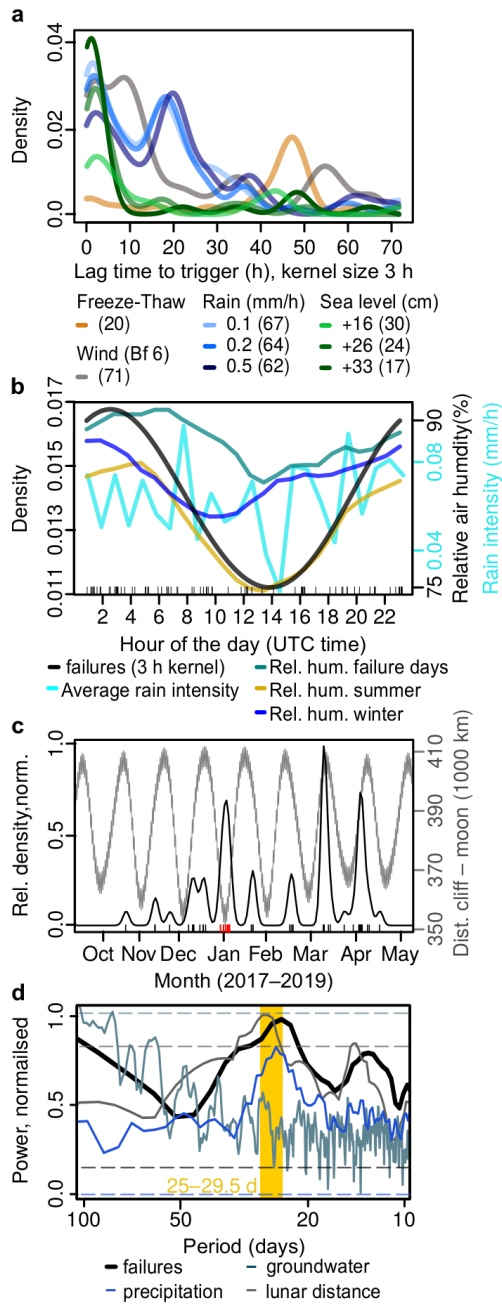


Figure 6. Drivers and triggers of cliff failures on Jasmund. a) Kernel density estimates (72 h duration) of time lags between triggers and failures. Values in parentheses denote number of failures within 72 h. b) Diurnal failure activity density estimate (black line), relative air humidity, and average diurnal precipitation intensity. c) Seasonal failure density estimates (period 2017–2019). Rugs along the x axis denote individual failures (red rugs indicate anomalous failure phase around the year end 2018). Grey curve shows lunar distance, i.e., distance between the gravity centre of the moon and the cliff area. d) Spectra of cliff failures and potential drivers. Lunar distance, precipitation and failures share a common periodicity window (orange polygon) at 25–29.5 days. Horizontal dashed lines depict significance thresholds for the spectra.

607 4.4 Biotic cliff preconditioning

608 There is an important seasonal effect that preconditions the Jasmund cliff system
 609 for failure on shorter, lunar (Fig. 6 c) and diurnal (Fig. 6 a-b) time scales. Although we
 610 lacked seismic evidence of cliff failures during the summer periods when no sensors were
 611 operational, we recorded only minor released volumes based on the UAV data (236 and
 612 389 m³, respectively), indicating that the summer periods were likely less active than
 613 the November–May windows. We attribute this seasonal pattern to water uptake by the
 614 dense beech forest covering the cliff hinterland. On Jasmund, the vegetative season typ-
 615 ically starts in early May and ends in October–November. During this season, water up-
 616 take by trees leads to progressive drying of the subsurface beyond the recharge capac-
 617 ity of summer rain. Beech trees can transpire hundreds of litres of soil water per day (Střelcová
 618 et al., 2002), leading to prolonged negative water potentials during the vegetative sea-
 619 son. In a beech dominated natural forest in central Europe (Střelcová et al., 2002), soil
 620 water potential throughout the first 70 cm graded from -80 to -700 hPa between late spring
 621 and autumn. This prevents major lateral soil water movements during the vegetative sea-
 622 son. Moreover, leaves contribute about 30 % to evaporation of rain water before it reaches
 623 the ground (interception loss), further contributing to systematically drier soil conditions
 624 between spring and autumn (Friesen & Van Stan II, 2019). During vegetation dormancy,
 625 from November to May, water uptake by roots and interception loss is limited, and rain
 626 storms can optimally recharge the antecedent soil moisture budget (Fig. SI 2). Hence,
 627 we infer that there is a vegetation control on cliff stability on Jasmund, expressed on the
 628 seasonal scale, through the regulation of antecedent soil moisture.

629 The seasonal antecedent soil moisture cycle is supported by our data on near sur-
 630 face seismic wave velocities (Fig. 1 f). Since the dv/v values result from an inversion pro-
 631 cess that finds those values within a sliding time window that can best explain the change
 632 in the seismic properties, there is no uncertainty estimate associated with the results.
 633 However, overall similar trends in the dv/v time series of two stations standing more than
 634 a km apart from each other indicates a coherent forcing mechanism. Estimated dv/v val-
 635 ues of our two central seismic stations were high by the end of the vegetative season and
 636 started to decline around November, before rising again in late spring. We attribute this
 637 to drying of the near-surface substrate in summer, and wetting in winter. Relative wave
 638 velocity increases as the ground material becomes more rigid (or when its temperature
 639 increases; Clements & Denolle, 2018) and vice versa. In the case of the chalk from our
 640 study region, rigidity is strongly controlled by moisture content, and less so by temper-
 641 ature changes, especially at several decimetres depth and under a dense beech canopy.
 642 These dv/v trends were not consistent with the groundwater levels, which fluctuated by
 643 about one meter at a depth of about 15 m below the surface, suggesting that our wave
 644 velocity monitoring was mostly sensitive to near surface soil moisture content. Moreover,
 645 in the long term, groundwater levels (see SI for details) vary not only at the annual scale
 646 (about 0.2–0.3 m amplitude of change) but more drastically at the multi-year scale (up
 647 to 1.5 m amplitude of change during the last decade), masking annual effects completely.
 648 Our instrumented period captures one such large scale effect: the above-average wet year
 649 of 2017 resulted in a groundwater high-stand while the above average dry year of 2018
 650 caused a local low-stand of groundwater (Fig. 1 e) independent of smaller amplitude changes
 651 at the seasonal scale.

652 4.5 Multi-year scale of cliff activity

653 We identified a legacy of climatic boundary conditions, expressed in a large num-
 654 ber and volume of cliff failures in winter 2017/18 after a wet summer with 126 % of av-
 655 erage seasonal precipitation (117 % in the subsequent winter), and a smaller failure num-
 656 ber and volume in winter 2018/19 after a dry summer with only 51 % (97 % in the sub-
 657 sequent winter) of the average precipitation. Whether the effect is driven by the sum-
 658 mer period, with more intense deviations from the average patterns, or the winter pe-

659 riod with less (2018) to negligible (2019) deviations, remains elusive from our data. How-
 660 ever, in light of the above explained effect that vegetation causes overall dry soil con-
 661 ditions during summer and allows the restoration of sufficient moisture conditions pre-
 662 dominantly during winter dormancy, it appears more likely that it is the summer period
 663 that sets the boundary conditions for the subsequent winter period of cliff failure den-
 664 sity.

665 Future climate projections for Jasmund include generally drier conditions and more
 666 variable precipitation events (Frei et al., 2006; Umweltbundesamt, 2015). With sustained
 667 moisture in the cliff and frequent precipitation being the dominant driver and trigger for
 668 failures identified in our study, the chalk cliffs may experience fewer failures as the de-
 669 creasing lateral water input fails to precondition the system to a state where rain and
 670 relative air humidity can trigger failures in the volume range witnessed during our study
 671 period. On the multi-year turn, this may result in a decreasing sediment supply via fail-
 672 ures to the cliff base and beach environment for uptake by waves agitating those deposits
 673 (cf. fig. 2 b and d, Stephensen, 2014). As a consequence, the erosive action of waves would
 674 extract more and more fine material from the beach instead, until the currently 2 m high
 675 ramp has become sufficiently lower and waves would be able to affect the cliff base di-
 676 rectly. Ultimately, the coast cliffs may become increasingly prone to wave action with
 677 possible undercutting, as the absence of a sediment apron and the proximity to break-
 678 ing waves makes them more prone to net basal erosion. This may eventually lead to less
 679 frequent but more catastrophic failures with significantly larger volumes, as failures would
 680 not initiate at $29.0^{+10.5}_{-16.0}$ m height and due to local destabilisation caused by a moisture-
 681 driven chalk state transition, but at the cliff base and due to destabilising process that
 682 penetrates deeper into the chalk material. Thus, although under generally drier condi-
 683 tions the rigidity of the cliff would increase, the failure volumes would increase, as well
 684 (see for example discussion by Dussauge et al., 2003). Unlike sandy beaches, cliffs are
 685 not able to recover after erosive events by aggradation of new material from other than
 686 cliff derived sources (Stephensen, 2014). Thus, there is no adjusting response mechanism
 687 in such an erosive system, which makes estimating the consequences of climate change
 688 for cliff coasts even more important.

689 5 Conclusions

690 We have used a combined seismic and UAV approach to gain new insight to dy-
 691 namics and triggers of coastal cliff activity, allowing the exploration of geomorphic re-
 692 lationships across a larger spatial and temporal range than would be possible with other
 693 existing techniques. This has revealed that, in the absence of strong tidal and wave forc-
 694 ing as direct triggers of failures, patterns and frequencies of cliff failures along the chalk
 695 coast of Jasmund, Germany, are affected by the presence of water in the cliff on a range
 696 of time scales. Water controls the rigidity of the material and causes a state transition,
 697 from solid towards liquid. This gives rise to distinct cycles of cliff failure at annual, sea-
 698 sonal, diurnal and possibly lunar time scales. Climatic effects set the baseline for fail-
 699 ure frequency, soil moisture uptake by trees suppresses failures in the vegetation period,
 700 precipitation causes failures by direct rain onto and groundwater flow towards the cliff,
 701 and higher atmospheric moisture levels may promote failures during the night. Failure
 702 deposits are typically amalgams and our seismic data reveals their formation from clus-
 703 ters of geomorphic activity rather than from single failures. Under increasingly drier cli-
 704 mate conditions, the cliff may grade into a (different) transient, characterized by less fre-
 705 quent small failures due to insufficient moisture preconditions, which in turn may pre-
 706 pare the cliff for more large events driven by erosion at the cliff base.

707 **Acknowledgments**

708 This research was made possible by the Helmholtz Impulse and Network Fund. The
 709 underlying data sets are provided under DOI 10.17605/OSF.IO/FV64X (<https://osf.io/fv64x/>).
 710 The analysis scripts are provided in the supporting information. Seismic data are avail-
 711 able via GEOFON data services. We thank Christopher Roettig and Sascha Meszner for
 712 the enlightening discussion on lunar influence on cliff activity and Björn Piltz for his in-
 713 put on lunar orbital parameters, as well as Theresa Blume for the suggested soil mois-
 714 ture input. An anonymous tractor driver is thanked for saving the spring 2018 survey
 715 mission. We thank the three reviewers and the editor for the thoughtful and construc-
 716 tive input.

717 **References**

- 718 Adderley, E. E., & Brown, E. G. (1962). Lunar component in precipitation data.
 719 *Science*, *749–750*, 137. doi: 10.1126/science.137.3532.749
- 720 Allen, R. (1982). Automatic phase pickers: Their present use and future prospects.
 721 *Bulletin of the Seismological Society of America*, *72*, S225–S242.
- 722 Bradley, D. A., Woodbury, M. A., & Brier, G. W. (1962). Lunar synodical and
 723 widespread precipitation. *Science*, *748–749*, 137. doi: 10.1126/science.137.3532
 724 .748
- 725 Briciu, A.-E. (2014). Wavelet analysis of lunar semidiurnal tidal influence on se-
 726 lected inland rivers across the globe. *Scientific Reports*, *4*, 4193.
- 727 Burtin, A., Hovius, N., Milodowski, D. T., Chen, Y.-G., Wu, Y.-M., Lin, C.-W., ...
 728 Leu, P.-L. (2013). Continuous catchment-scale monitoring of geomorphic pro-
 729 cesses with a 2-d seismological array. *Journal of Geophysical Research Earth*
 730 *Surface*, *118*, 19561974. doi: 10.1002/jgrf.20137
- 731 Burtin, A., Hovius, N., & Turowski, J. M. (2016). Seismic monitoring of torrential
 732 and fluvial processes. *Earth Surface Dynamics*, *4*, 285–307. doi: 10.5194/esurf
 733 -4-285-2016
- 734 Cerveny, R., Svoma, B., & Vose, R. (2010). Lunar tidal influence on inland river
 735 streamflow across the conterminous united states. *Geophysical Research Let-*
 736 *ters*, *37*(L22406). doi: 10.2916/2010GL045564
- 737 Clements, T., & Denolle, M. A. (2018). Tracking groundwater levels using the am-
 738 bient seismic field. *Geophysical Research Letters*, *45*(13), 6459–6465. doi: 10
 739 .1029/2018GL077706
- 740 Collins, B., & Sitar, N. (2008). Processes of coastal bluff erosion in weakly lithified
 741 sands, pacifica, california, usa. *Geomorphology*, *97*, 483 – 501. doi: 10.1016/j
 742 .geomorph.2007.09.004
- 743 Collins, B., & Stock, G. (2016). Rockfall triggering by cyclic thermal stressing of ex-
 744 foliation fractures. *Nature Geoscience*, *9*, 395–400.
- 745 Cook, K., & Dietze, M. (2019). Short communication: A simple workflow for robust
 746 low-cost UAV-derived change detection without ground control points. *Earth*
 747 *Surface Dynamics*, *7*(4), 1009–1017. Retrieved from [https://www.earth-surf](https://www.earth-surf-dynam.net/7/1009/2019/)
 748 [-dynam.net/7/1009/2019/](https://www.earth-surf-dynam.net/7/1009/2019/) doi: 10.5194/esurf-7-1009-2019
- 749 Dietze, M. (2018a). 'eseis' – an R software toolbox for environmental seismology. v.
 750 0.4.0. GFZ Data services. doi: <http://doi.org/10.5880/GFZ.5.1.2018.001>
- 751 Dietze, M. (2018b). The R package eseis a software toolbox for environmental seis-
 752 mology. *Earth Surface Dynamics*, *6*, 669–686. doi: 10.5194/esurf-6-669-2018
- 753 Dietze, M., Kreutzer, S., Burow, C., Fuchs, M. C., Fischer, M., & Schmidt, C.
 754 (2016). The abanico plot: Visualising chronometric data with individual
 755 standard errors. *Quaternary Geochronology*, *31*, 12–18.
- 756 Dietze, M., Mohadjer, S., Turowski, J., Ehlers, T., & Hovius, N. (2017). Validity,
 757 precision and limitations of seismic rockfall monitoring. *Earth Surface Dynam-*
 758 *ics*, *2017*, 1–23. doi: 10.5194/esurf-2017-12

- 759 Dietze, M., Turowski, J. M., Cook, K. L., & Hovius, N. (2017). Spatiotemporal pat-
760 terns, triggers and anatomies of seismically detected rockfalls. *Earth Surface*
761 *Dynamics*, 5(4), 757–779. Retrieved from [https://www.earth-surf-dynam](https://www.earth-surf-dynam.net/5/757/2017/)
762 [.net/5/757/2017/](https://www.earth-surf-dynam.net/5/757/2017/) doi: 10.5194/esurf-5-757-2017
- 763 Duperret, A., Taibi, S., Mortimore, R., & Daigneault, M. (2005). Effect of
764 groundwater and sea cycles on the strength of chalk rock from unsta-
765 ble coastal cliffs of nw france. *Engineering Geology*, 78, 321–343. doi:
766 10.1016/j.enggeo.2005.01.004
- 767 Dussauge, C., Grasso, J.-R., & Helmstetter, A. (2003). Statistical analysis of rockfall
768 volume distributions: Implications for rockfall dynamics. *Journal of Geophysi-*
769 *cal Research: Solid Earth*, 108(B6). doi: 10.1029/2001JB000650
- 770 DWD. (2019). *Climate Data Centre*. Retrieved from [https://www.dwd.de/EN/](https://www.dwd.de/EN/climate_environment/cdc/cdc_node.html)
771 [climate_environment/cdc/cdc_node.html](https://www.dwd.de/EN/climate_environment/cdc/cdc_node.html)
- 772 Frei, C., Schöll, R., Fukutome, S., Schmidli, J., & Vidale, P. (2006). Future change
773 of precipitation extremes in europe: Intercomparison of scenarios from re-
774 gional climate models. *Journal of Geophysical Research*, 111(D06105). doi:
775 10.1029/2005JD005965
- 776 Friesen, J., & Van Stan II, J. (2019). Early european observations of precipita-
777 tion partitioning by vegetation: A synthesis and evaluation of 19th century
778 findings. *Geosciences*, 9, 1–20. doi: 10.3390/geosciences9100423
- 779 Garratt, J., & Segal, M. (1988). On the contribution of atmospheric moisture to
780 dew formation. *Boundary-Layer Meteorology*, 45, 209–236. doi: 10.1007/
781 BF01066671
- 782 Gehrman, A. (2018). *The multi-stage structural development of the upper we-*
783 *ichselian jasmund glacitectonic complex (rgen, ne germany)* (Unpublished
784 doctoral dissertation). University of Greifswald.
- 785 GPL. (2019). *Cloudcompare, v. 2.10.1*. doi: <http://www.cloudcompare.org/>
- 786 Helmstetter, A., & Garambois, S. (2010). Seismic monitoring of Sechilienne rockslide
787 (French Alps): Analysis of seismic signals and their correlation with rainfalls.
788 *Journal of Geophysical Research*, 115, F03016. doi: 10.1029/2009JF001532
- 789 Hibert, C., Mangeney, A., Grandjean, G., Baillard, C., Rivet, D., Shapiro, N. M.,
790 ... Crawford, W. (2014). Automated identification, location, and volume
791 estimation of rockfalls at Piton de la Fournaise volcano. *Journal of Geophysical*
792 *Research*, 119, 1082–1105. doi: 10.1002/2013JF002970
- 793 Hibert, C., Mangeney, A., Grandjean, G., & Shapiro, N. M. (2011). Slope in-
794 stabilities in Dolomieu crater, Reunion Island: From seismic signals to rock-
795 fall characteristics. *Journal of Geophysical Research*, 116, F04032. doi:
796 10.1029/2011JF002038
- 797 Holmes, T. R. H., Owe, M., De Jeu, R. A. M., & Kooi, H. (2008). Estimat-
798 ing the soil temperature profile from a single depth observation: A sim-
799 ple empirical heatflow solution. *Water Resources Research*, 44(2). doi:
800 10.1029/2007WR005994
- 801 Inkenbrandt, P., Doss, P., Pickett, T., & Brown, R. (2005). Barometric and earth-
802 tide induced water-level changes in the inglefield sandstone in southwestern
803 indiana. *Proceedings of the Indiana Academy of Science*, 114, 1–8.
- 804 IZW. (2003). *Die Küste*. Retrieved from [https://izw.baw.de/die-kueste/0/](https://izw.baw.de/die-kueste/0/k066102.pdf)
805 [k066102.pdf](https://izw.baw.de/die-kueste/0/k066102.pdf)
- 806 JPL. (2019). Retrieved from <https://ssd.jpl.nasa.gov/horizons.cgi>
- 807 Kennedy, D. M., Coombes, M. A., & Mottershead, D. N. (2017). The temporal and
808 spatial scales of rocky coast geomorphology: a commentary. *Earth Surf. Pro-*
809 *cess. Landforms*, 42, 1597–1600. doi: 10.1002/esp.4150
- 810 Kogure, T., Aoki, H., Maekado, A., Hirose, T., & Matsukura, Y. (2006). Effect
811 of the development of notches and tension cracks on instability of limestone
812 coastal cliffs in the ryukyus, japan. *Geomorphology*, 80, 236–244. doi:
813 10.1016/j.geomorph.2006.02.012

- 814 Krienke, K., & Koepke, C. (2006). Landslides at the sea cliffs of the Isle of Rügen
815 (northeast Germany) during the winter of 2004/05 – geology and soil mechan-
816 ics. *Zeitschrift für geologische Wissenschaften*, *34*, 105-113.
- 817 Lague, B. N., D., & Leroux, J. (2013). Accurate 3D comparison of complex topog-
818 raphy with terrestrial laser scanner: Application to the Rangitikei canyon (nz).
819 *ISPRS J. Photogramm.*, *82*, 10–26. doi: 10.1016/j.isprsjprs.2013.04.009
- 820 Larose, E., Carrière, S., Voisin, C., Bottelin, P., Baillet, L., Guguen, P., ... Massey,
821 C. (2015). Environmental seismology: What can we learn on earth surface
822 processes with ambient noise? *Journal of Applied Geophysics*, *116*, 62–74. doi:
823 10.1016/j.jappgeo.2015.02.001
- 824 Lethbridge, M. D. (1990). Thunderstorms, cosmic rays, and solar-lunar influences.
825 *Journal of Geophysical Research: Atmospheres*, *95*(D9), 13645-13649. doi: 10
826 .1029/JD095iD09p13645
- 827 Letortu, P., Costa, S., Cadot, J., Coinaud, C., & Cantat, O. (2015). Statistical
828 and empirical analyses of the triggers of coastal chalk cliff failure. *Earth Sur-
829 face Processes and Landforms*(40), 1371-1386. doi: 10.1002/esp.3741
- 830 Lim, M., Rosser, N., Allison, R., & Petley, D. (2010). Erosional processes in the
831 hard rock coastal cliffs of Staithes, North Yorkshire. *Geomorphology*, *114*, 12–
832 21.
- 833 LUNG. (2019). Retrieved from [https://www.lung.mv-regierung.de/insite/cms/
834 umwelt/geologie/rohstoffgeologie/rohstoffgeologie_kreidekalk.htm](https://www.lung.mv-regierung.de/insite/cms/umwelt/geologie/rohstoffgeologie/rohstoffgeologie_kreidekalk.htm)
- 835 Menatschi, L., Voudoukas, M., Pekel, J.-F., Voukouvalas, E., & Feyen, L. (2018).
836 Global long-term observations of coastal erosion and accretion. *Scientific Re-
837 ports*, *8*, 12876.
- 838 Meng, H., & Ben-Zion, Y. (2018). Characteristics of airplanes and helicopters
839 recorded by a dense seismic array near Anza California. *Journal of Geophysical
840 Research: Solid Earth*, *123*(6), 4783-4797. doi: 10.1029/2017JB015240
- 841 Obst, K., & Schütze, K. (2005). Analysis of cliff slides at the steep coast of Jas-
842 mund, Rügen in 2005. *Zeitschrift für geologische Wissenschaften*, *34*, 11-37.
- 843 Rosser, N., Brain, M., Petley, D., Lim, M., & Norman, E. (2013). Coastline retreat
844 via progressive failure of rocky coastal cliffs. *Geology*, *41*(8), 939-942.
- 845 Rosser, N., Lim, M., Petley, D., Dunning, S., & Allison, R. (2007). Patterns of
846 precursory rockfall prior to slope failure. *Journal of Geophysical Research*,
847 *112*(F04012). doi: 10.1029/2006JF000642
- 848 Roy, S. (2006). Impact of lunar cycle on the precipitation in India. *Geophysical Re-
849 search Letters*, *33*, L01707. doi: 10.1029/2005GL024771
- 850 Sens-Schönfelder, C. (2014). *Monitoring and Imaging based on Interferometric con-
851 cepts package*. Retrieved from <https://github.com/miic-sw/miic>
- 852 Sens-Schönfelder, C., & Wegler, U. (2006). Passive image interferometry and sea-
853 sonal variations of seismic velocities at Merapi volcano, Indonesia. *Geophysical
854 Research Letters*, *33*(21).
- 855 Snieder, R. (2004). Extracting the Green's function from the correlation of coda
856 waves: A derivation based on stationary phase. *Phys. Rev. E*, *69*, 046610. doi:
857 10.1103/PhysRevE.69.046610
- 858 STALUVP. (2019). *Groundwater log time series, Buddenhagen, Rügen*.
- 859 Stephensen, W. (2014). Rock Coasts. In D. Masselink & R. Gehrels (Eds.), *Coastal
860 Environments and Global Change* (first edition ed., p. 256-379). John Wiley &
861 Sons.
- 862 Stock, G., Collins, B., Santaniello, D., Zimmer, V., Wiczorek, G., & Snyder, J.
863 (2013). Historical rock falls in Yosemite National Park. *U.S. Geological Survey
864 Data Series 746*, *746*, 17.
- 865 Štrélcová, K., Matejka, F., & Mindáš, J. (2002). Estimation of beech tree transpira-
866 tion in relation to their social status in forest stand. *Journal of Forest Science*,
867 *48*, 130–140.
- 868 Umweltbundesamt. (2015). *Germany's vulnerability to climate change*. Retrieved

- 869 from [https://www.umweltbundesamt.de/sites/default/files/medien/](https://www.umweltbundesamt.de/sites/default/files/medien/378/publikationen/climate_change_24_2015_summary_vulnerabilitaet_deutschlands_gegenueber_dem_klimawandel_2.pdf)
870 [378/publikationen/climate_change_24_2015_summary_vulnerabilitaet](https://www.umweltbundesamt.de/sites/default/files/medien/378/publikationen/climate_change_24_2015_summary_vulnerabilitaet_deutschlands_gegenueber_dem_klimawandel_2.pdf)
871 [_deutschlands_gegenueber_dem_klimawandel_2.pdf](https://www.umweltbundesamt.de/sites/default/files/medien/378/publikationen/climate_change_24_2015_summary_vulnerabilitaet_deutschlands_gegenueber_dem_klimawandel_2.pdf)
- 872 Vann Jones, V., Rosser, N., Brain, M., & Petley, D. (2015). Quantifying the environ-
873 mental controls on erosion of a hard rock cliff. *Marine Geology*, *363*, 230–242.
874 doi: 10.1016/j.margeo.2014.12.008
- 875 Voake, T., Nermoen, A., Ravns, C., Korsnes, R., & Fabricius, I. (2019). Influence
876 of temperature cycling and pore fluid on tensile strength of chalk. *Journal of*
877 *Rock Mechanics and Geotechnical Engineering*, *11*(2), 277 - 288. doi: [https://](https://doi.org/10.1016/j.jrmge.2018.12.004)
878 doi.org/10.1016/j.jrmge.2018.12.004
- 879 Wiczonek, G. (1996). Landslide triggering mechanisms. In A. Turner & R. Schuster
880 (Eds.), *Landslides – investigation and mitigation* (pp. 76–90). Transportation
881 Research Board, National Research Council, National Academy Press.
- 882 Williams, D. (2016). Chapter 37 - tailings storage facilities. In M. Adams (Ed.),
883 *Gold Ore Processing* (Second Edition ed., pp. 663–676). Elsevier. doi: [https://](https://doi.org/10.1016/B978-0-444-63658-4.00037-2)
884 doi.org/10.1016/B978-0-444-63658-4.00037-2
- 885 WSV. (2019). Retrieved from <http://www.pegelonline.wsv.de>
- 886 Young, A., & Carilli, J. (2019). Global distribution of coastal cliffs. *Earth Surface*
887 *Processes and Landforms*, *44*, 1309–1316.